

High-rate, high-fidelity entanglement of qubits across an elementary quantum network

L. J. Stephenson,* D. P. Nadlinger,* B. C. Nichol, S. An, P. Drmota,

T. G. Ballance,† K. Thirumalai, J. F. Goodwin, D. M. Lucas, and C. J. Ballance‡

Department of Physics, University of Oxford, Clarendon Laboratory, Parks Road, Oxford OX1 3PU, U.K.

(Dated: May 12, 2020)

We demonstrate remote entanglement of trapped-ion qubits via a quantum-optical fibre link with fidelity and rate approaching those of local operations. Two $^{88}\text{Sr}^+$ qubits are entangled via the polarisation degree of freedom of two spontaneously emitted 422 nm photons which are coupled by high-numerical-aperture lenses into single-mode optical fibres and interfere on a beam splitter. A novel geometry allows high-efficiency photon collection while maintaining unit fidelity for ion-photon entanglement. We generate heralded Bell pairs with fidelity 94% at an average rate 182 s^{-1} (success probability 2.18×10^{-4}).

The ability to form logical connections between all quantum bits (qubits) of a quantum processor is a prerequisite for building a fault-tolerant universal device [1]. Trapped atomic ions have been identified as an excellent candidate qubit technology because they allow the implementation of single-qubit operations [2–4], two-qubit phonon-mediated gates [3, 4] and quantum memories [5, 6], all with high fidelity. However, the number of ions that can be reliably interfaced in a single trap is limited by the motional mode density, necessitating architectures with multiple trap zones each hosting comparatively few ions. Trap zones can be interfaced by physically shuttling qubits across centimetre-scale distances using electric fields [7], or by using photons to distribute entanglement over larger distances [8]. Photonic entanglement could also increase the connectivity of trapped-ion qubits via dynamically switchable fibre links [9], or allow the interfacing of different qubit platforms [10]. It also enables other quantum networking applications such as quantum key distribution, teleportation of quantum states, and blind quantum computing [11, 12]. For ions, the entanglement rate is limited fundamentally only by the photon scattering rate ($\sim 100\text{ MHz}$), exceeding local multiqubit operation rates (motional gates [13] and shuttling [14, 15]) at typical secular trap frequencies ($\sim 1\text{ MHz}$). In practice, photonic entanglement rates have been far lower than this, limited principally by low photon collection efficiencies [16]; the highest previously reported rate for ions was 4.5 s^{-1} , with 78% fidelity [17]. Faster rates have been achieved with nitrogen-vacancy centres (39 Hz) and quantum dots (7.3 kHz), with fidelity $\approx 60\%$ [18, 19]. Heralded entanglement of remote qubits with fidelity above 90% has not previously been reported for any physical systems at rates above a few millihertz [20–22].

In this Letter, we report the generation of entanglement between two qubits in separate ion traps at rates and fidelities approaching those of typical local (intratrap) operations, by swapping entanglement between photons emitted by the ions onto the ions themselves [23]. At these higher rates and fidelities, distillation procedures based on photonic entanglement [24] start to be-

come a viable method for creating high quality entanglement across a scalable trapped-ion quantum computer.

A novel excitation scheme using $^{88}\text{Sr}^+$ ions with photon collection perpendicular to the static applied magnetic field allows an increased rate over previous experiments [17], with polarisation mixing maximally suppressed by coupling into a single mode optical fibre. In contrast to previous schemes using $^{171}\text{Yb}^+$, the collection geometry does not impede the use of beams parallel to the applied magnetic field. This allows standard σ -polarised optical pumping to be employed, thus permitting a wider choice of ion species and the straightforward initialisation of multiple ion species in a single trap.

We collect photons from the spontaneous decay of the excited electronic state $|5p P_{1/2}, m = +1/2\rangle$ of $^{88}\text{Sr}^+$, as shown in Fig. 1(a). Decays to the two states of the ground level $5s S_{1/2}$ are associated with π and σ^+ polarised photons, forming an entangled ion-photon state given by

$$|\psi\rangle = \sqrt{\frac{2}{3}} |\downarrow\rangle |\sigma^+\rangle + \sqrt{\frac{1}{3}} |\uparrow\rangle |\pi\rangle,$$

where the weightings are due to the Clebsch-Gordan coefficients for each decay path, and the ion qubit states are labeled with $|\downarrow\rangle$ and $|\uparrow\rangle$. Perpendicular to the magnetic field axis, the emitted field from the π decay has twice the intensity, and so for photons on the collection axis the ion-photon state is

$$|\psi\rangle = \frac{1}{\sqrt{2}} (|\downarrow\rangle |H\rangle + |\uparrow\rangle |V\rangle), \quad (1)$$

where σ^+ and π have been relabeled H and V to emphasise that the two photon polarisations are both linear and orthogonal; note that this is a maximally entangled Bell state.

The nonorthogonality of the σ^+ and π emissions away from the collection axis would normally reduce the fidelity of the ion-photon entanglement at the high numerical apertures needed to maximise the photon collection efficiency [25]. However, with the chosen collection geometry, coupling into a single mode optical fibre rejects the nonorthogonal component of the σ^+ emission,

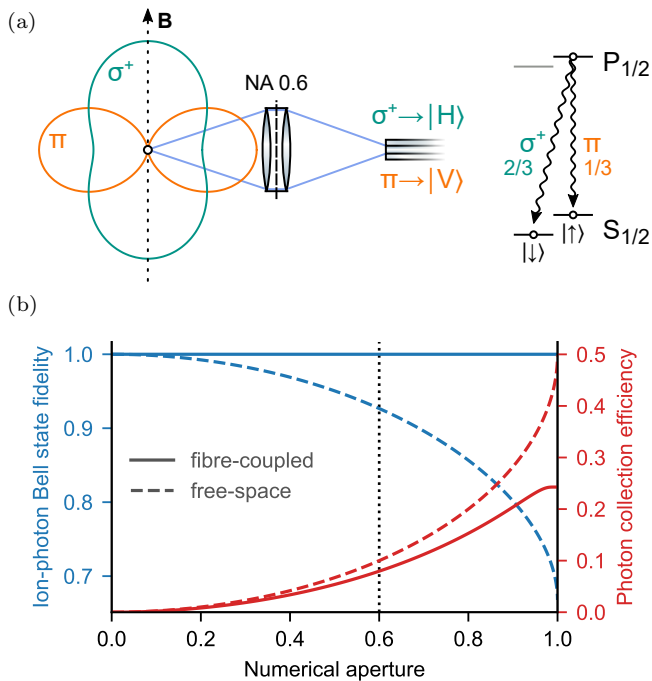


FIG. 1. (a) Intensity distribution of the light field for σ^+ and π decay channels, relative to the quantisation axis set by the static magnetic field \mathbf{B} , and the branching fractions for each decay due to atomic selection rules. At the fibre input face, photons from σ^+ (π) fibre polarisation mode. (b) Maximum fraction of photons emitted by the ion that can be collected (red) and theoretical ion-photon entanglement fidelity (blue) versus collection optic numerical aperture. For free-space collection (dashed lines) polarisation mixing leads to a loss in fidelity with increasing numerical aperture. To model the fibre-coupling (solid lines), we calculate the overlap of the light field with a Gaussian mode on the dashed plane in (a): a smaller fraction of the emission is collected, but the polarisation mixing is completely suppressed. The vertical dashed line shows the NA 0.6 used in this Letter, where the fibre collection efficiency is 80% of that in free space.

reducing the maximum possible collection efficiency but maintaining unit ion-photon Bell state fidelity independent of collection aperture [see Fig. 1(b)]. In contrast to other schemes, no photons of comparable wavelength are produced from undesired decay channels. This eliminates the need to filter out such photons [26], enabling higher rates to be achieved with our collection geometry and excitation scheme.

By collecting two such photons entangled with separated ions and erasing the which-path information from the photons, a projective measurement of the two-photon state in the Bell basis will herald the projection of the two ions into a corresponding Bell state [27].

In our experiment, $^{88}\text{Sr}^+$ ions are trapped in two identical, high-optical-access, microfabricated surface traps [28] in two vacuum systems, designated “Alice”

and “Bob”, separated by 2 m. In each system, a high-numerical-aperture (NA 0.6) lens, aligned perpendicular to the applied magnetic field of 0.56 mT, couples single photons from the ion into an antireflection (AR) coated single-mode optical fibre. Non-polarisation-maintaining (non-PM) fibres are used so as to introduce minimal differential phase between H and V photons (PM fibres introduce a large, temperature-sensitive, differential phase which would be difficult to control). A second objective (NA 0.3) images the ion through a slot in the trap onto a photomultiplier tube for fluorescence detection.

The relevant electronic structure of $^{88}\text{Sr}^+$ is shown in Fig. 2. Ions are Doppler cooled with lasers at 422 nm and 1092 nm. The Zeeman structure of the ground level is used to encode the “Zeeman” qubit: $|S_{1/2}, m = -1/2\rangle = |\downarrow\rangle$ and $|S_{1/2}, m = +1/2\rangle = |\uparrow\rangle$. We also define an “optical” qubit between the metastable level $|4d D_{5/2}, m = -3/2\rangle = |D\rangle$ and $|\downarrow\rangle$, and use a narrow linewidth laser at 674 nm to coherently transfer population between either of the Zeeman qubit states and $|D\rangle$, for ion state tomography. As $|D\rangle$ is outside the Doppler cooling cycle, it can also be used to shelve population from $|\uparrow\rangle$ to measure the ground state qubit by state-dependent fluorescence detection [29].

The experimental sequence for generating entangled photons is shown in Fig. 2. An optimised attempt section at rate 1 MHz, lasting at most 500 μs , is interleaved with 100 μs of Doppler cooling, until detection of an appropriate two-photon coincidence heralds the creation of ion-ion entanglement. (In single-ion/single-photon experiments, a single click of a chosen detector instead breaks this attempt loop and triggers the start of the analysis sequence.) The sequence is controlled by an FPGA [30], incorporating the custom-optimised, precompiled section with decision branching in hardware, and just-in-time compiled sequences for qubit manipulations.

The projective measurement of the photons is performed with a partial Bell state analyser, consisting of a 50:50 non-polarising beam splitter (NPBS) and polarising beam splitters (PBSs) on each output arm. All four output channels are monitored by avalanche photodiodes (APDs, quantum efficiency 65% [31]), as shown in Fig. 3. Spatial mode matching of the photons from each system at the NPBS is aided by recoupling the light into AR-coated single-mode optical fibres before the APDs (coupling efficiency $\approx 90\%$). The total click efficiency into all APDs is typically 2.1% and 2.4% for Alice and Bob, respectively. These measured efficiencies imply that the mode matching into the first fibre is $\gtrsim 50\%$ of the theoretical optimum [8.0%, Fig. 1(b)].

We first characterise the entanglement between the ion and emitted photon for each of the trap systems, using one detector in the apparatus shown in Fig. 3. We perform full tomography of the combined ion-photon state by independently rotating each qubit. Rotations of the ion state are performed on the optical qubit using the

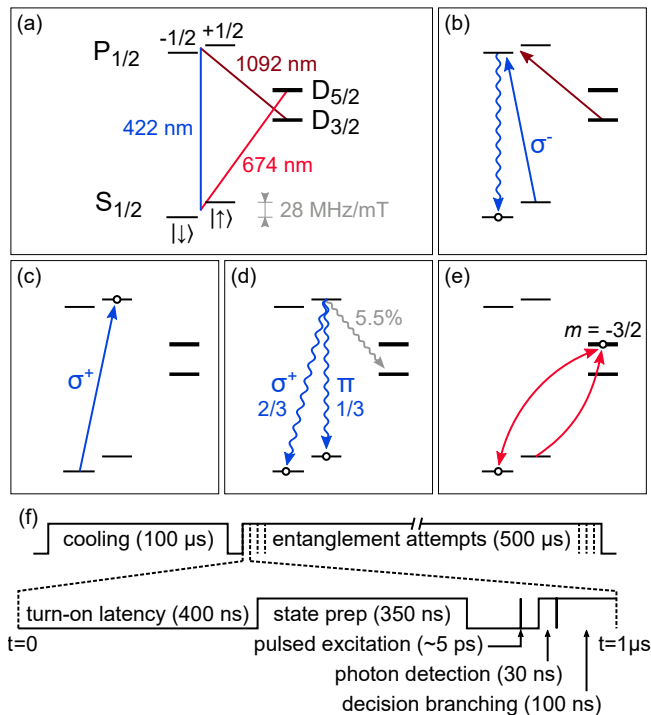


FIG. 2. (a) $^{88}\text{Sr}^+$ level diagram (not to scale). (b) The initial state preparation consists of optical pumping on the 422 nm transition, with a repumper at 1092 nm to clear the $D_{3/2}$ level. (c) A single ~ 5 ps pulse from a frequency-doubled mode-locked Ti:sapphire laser coherently transfers the population to $P_{1/2}$, $m = +1/2$ with $\approx 97\%$ probability. (d) The ion decays to a superposition of $|\downarrow\rangle$ and $|\uparrow\rangle$, emitting a photon whose polarisation state is entangled with the state of the ion. Decays to the $D_{3/2}$ manifold occur with probability 5.5%, but as the 1092 nm photons are not transmitted by the fibre, the only effect is to lower the overall rate. (e) Coherent manipulations are performed on the 674 nm transition to $|D\rangle$ in order to analyse the final ion qubit state. (f) Experimental sequence: the ions are Doppler cooled for 100 μs before the attempt loop (lasting up to 500 μs) begins. The enlarged view shows a single attempt, with ≈ 400 ns of latency between state preparation turn-on signal (at $t = 0$) and light arriving at the ion. State preparation (≈ 350 ns) is followed by a 100 ns delay to ensure that the beams are fully extinguished before the pulsed excitation. The 30 ns photon detection window begins 30 ns after the excitation pulse to allow for detector latency. A further 100 ns is required to decide whether to branch out of the attempt loop, in the event that a herald pattern is detected.

674 nm laser after mapping $|\uparrow\rangle$ to $|D\rangle$ with a π pulse. Rotations of the photon state are performed using the wave plates on the Bell state analyser. An overcomplete set of ion and photon measurements is used to characterise the entangled ion-photon state, and to calculate the maximum-likelihood estimate (MLE) of the composite density matrix. The density matrices obtained indicate a fidelity of 97.90(12)% [97.70(12)%] with the maximally entangled state, at an average rate of $4.0 \times 10^3 \text{ s}^{-1}$

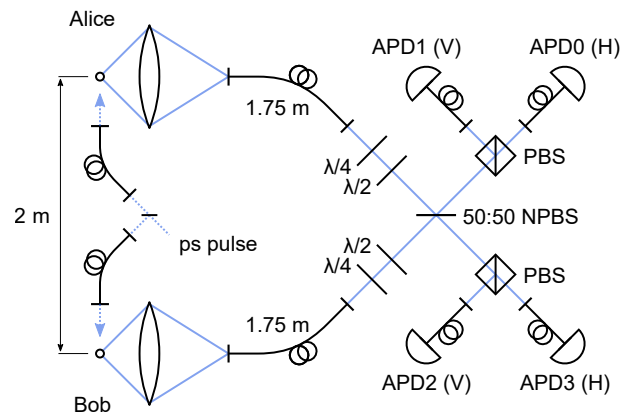


FIG. 3. Overview of apparatus. Single pulses from a frequency-doubled mode-locked laser are split to simultaneously excite ions in Alice and Bob. The spontaneously emitted photons are collected into single-mode non-PM fibres, with wave plates directly after the fibres to rotate the polarisation. The photons are then overlapped on a 50:50 NPBS, and detected on single-mode-fibre-coupled APDs following PBSs. To minimise the polarisation dependence of the NPBS, we use a small angle of incidence ($\approx 10^\circ$). The same apparatus is used for single-ion/single-photon experiments.

($5.7 \times 10^3 \text{ s}^{-1}$) for the Alice (Bob) system.

Ion qubit rotation errors account for $\approx 0.6\%$ of the total error, at $\approx 0.3\%$ per rotation. We measure correlations of ion state with photon polarisation of $P(\uparrow|V) \approx P(\downarrow|H) \approx 0.995$, which includes the error from one π pulse on the ion qubit. This bounds the error due to all polarisation mixing effects to $\lesssim 0.2\%$. Excited state preparation errors (preparing $|P_{1/2}, m = -1/2\rangle$ instead of $|P_{1/2}, m = +1/2\rangle$) depend on the polarisation impurity of both the optical pumping and pulsed excitation beams and are therefore suppressed. The remaining 1.4% error is attributed to ion qubit dephasing during the 60 μs delay between photon detection and tomography, and is expected to be due to noise in the applied magnetic field.

To entangle the two remote ion qubits, we erase the path information of photons entangled with each ion and subsequently project the ion-ion state via a destructive measurement on the photon polarisations. A coincidence detection on an appropriate pair of detectors heralds one of two Bell states: $|\Psi_{\text{photon}}^+\rangle := (|VH\rangle + |HV\rangle)/\sqrt{2}$ if the detectors are on the same output port of the NPBS, and $|\Psi_{\text{photon}}^-\rangle := (|VH\rangle - |HV\rangle)/\sqrt{2}$ if the detectors are on different output ports. Detection of $|\Psi_{\text{photon}}^\pm\rangle$ projects the ions correspondingly into $|\Psi_{\text{ion}}^\pm\rangle := (|\uparrow\downarrow\rangle \pm e^{i\phi}|\downarrow\uparrow\rangle)/\sqrt{2}$, where the phase ϕ is stable [32] and can be transformed to zero with local operations.

The probability of successfully heralding an entangle-

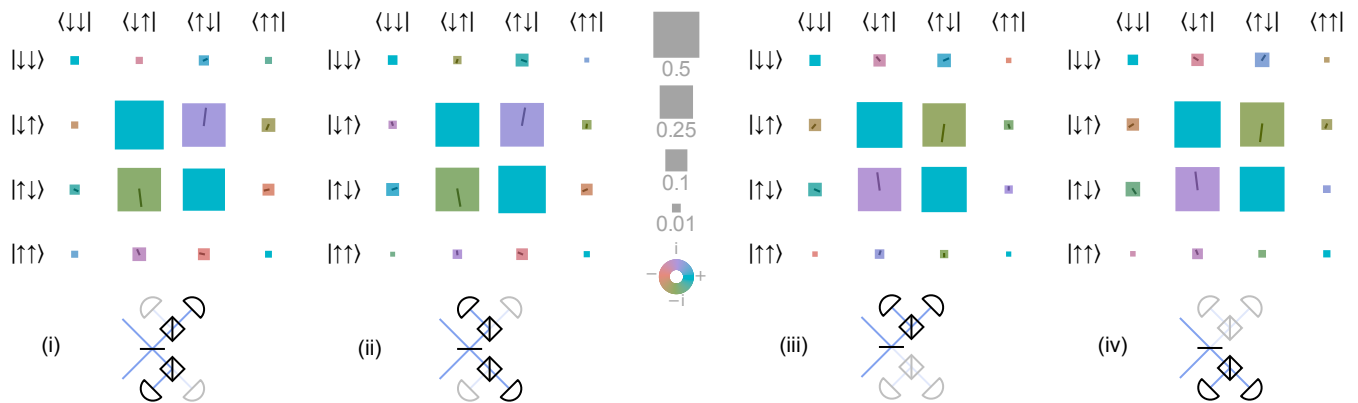


FIG. 4. The remote ion-ion density matrices and corresponding herald patterns (i)–(iv) as per the detector arrangement in Fig. 3. Detector clicks on opposing sides of the 50:50 beamsplitter (i), (ii) herald projection into $|\Psi_{\text{ion}}^{-}\rangle$, while clicks on the same side (iii), (iv) herald $|\Psi_{\text{ion}}^{+}\rangle$. The average fidelity of all four patterns to the nearest maximally entangled state is 94.0(5)%, at a heralded rate of 182 s^{-1} . (In this diagram the area of each square gives the magnitude of the matrix element, with the color representing the complex phase, according to the key shown. A “clock hand” also indicates the phase on the same color wheel. See the Supplemental Material for numerical information.)

ment event is given [17] by

$$P = p_{\text{Bell}} [P_{\downarrow} P_e P_S \bar{P}_{\text{click}}]^2, \quad (2)$$

where $p_{\text{Bell}} = 1/2$ because we have valid heralds only for two of the four possible two-photon Bell states, $P_{\downarrow} \approx 0.99$ is the probability of preparing the correct ground state before excitation, $P_e \approx 0.97$ is the population transferred to the excited state by the pulsed excitation beam, $P_S \approx 0.95$ is the probability of decaying to the $S_{1/2}$ ground states and $\bar{P}_{\text{click}} \approx 0.023$ is the average probability of detecting a photon emitted by an ion. We measure $P = 2.18 \times 10^{-4}$; given the average attempt rate (including Doppler cooling) of 833 kHz , P yields a heralded ion-ion entanglement rate of 182 s^{-1} .

After detection of a two-photon herald, we perform two-qubit tomography to verify the entangled state, using a series of single-qubit rotations and projective measurements [33]. The MLE ion-ion state is calculated for each of the four herald patterns individually, as shown in Fig. 4, indicating an average fidelity of 94.0(5)% to the closest maximally entangled state [34].

The total ion-ion infidelity is dominated by errors in the ion-photon fidelity from each trap as described above, totaling 4.4%, which includes errors in the ion-qubit rotations, ion dephasing, and polarisation mixing effects. Additional infidelities include: the measured imperfections of the beamsplitters in the Bell state analyser, $\lesssim 0.17\%$; temporal misalignment of the photons, $\lesssim 0.13\%$; and dark counts, which contribute $\lesssim 0.05\%$ despite a relatively high dark count rate of $\sim 60\text{ s}^{-1}$ per APD. The error due to mismatch of the photon modes at the NPBS is bounded by the measured fidelity to $< 1.3(5)\%$, which is approximately consistent with independent measurements.

In summary, we have used a new combination of collection geometry and excitation scheme to demonstrate remote entanglement between two atomic ion qubits at much higher rates and fidelities than previously measured. The dominant infidelities arose from single-ion manipulations and spin decoherence, due to noise in the applied magnetic field and other known technical issues. An order of magnitude of rate improvement is feasible by reducing latencies and the duration of state preparation shown in Fig. 2. Further rate gains could exploit the quadratic dependence on detection efficiency P_{click} indicated by Eq. (2), by using detectors of higher quantum efficiency, improving the mode matching into the fibres or using higher numerical aperture lenses to increase collection efficiency. Significantly greater increases could in principle be realised by the use of a mirror close to the ion [35, 36], or via the Purcell enhancement provided by an optical cavity [37–40]. Typical optical fibre losses at 422 nm are 30 dB km^{-1} ; frequency down conversion to the telecommunications C band (1550 nm) [41] would allow the distribution of entanglement over much larger distances than in this experiment. The measured structure of the remote state produced is such that only two entangled pairs would be needed to distill a single remote entangled pair at or above 99% fidelity [42]. This would allow the photonic link to approach the performance of state-of-the-art local operations, enabling a variety of quantum networking applications.

We would like to thank Peter Maunz (Sandia National Laboratories) for supplying HOA2 ion traps, and the developers of ARTIQ [43]. B. C. N. and K. T. acknowledge funding from the U.K. National Physical Laboratory and the Defence Science and Technology Laboratory respectively. C. J. B. acknowledges support from a UKRI FL Fellowship, and is a Director of Oxford Ionics Ltd. This

work was supported by the U.K. EPSRC “Networked Quantum Information Technology” Hub and the E.U. Quantum Technology Flagship Project AQTION (No. 820495).

* These two authors contributed equally

† Present address: ColdQuanta UK Ltd, Oxford

‡ chris.ballance@physics.ox.ac.uk

- [1] D. P. DiVincenzo, The physical implementation of quantum computation, *Fortschr. Phys.* **48**, 771 (2000).
- [2] T. P. Harty, D. T. C. Allcock, C. J. Ballance, L. Guidoni, H. A. Janacek, N. M. Linke, D. N. Stacey, and D. M. Lucas, High-Fidelity Preparation, Gates, Memory, and Readout of a Trapped-Ion Quantum Bit, *Phys. Rev. Lett.* **113**, 220501 (2014).
- [3] C. J. Ballance, T. P. Harty, N. M. Linke, M. A. Sepiol, and D. M. Lucas, High-Fidelity Quantum Logic Gates Using Trapped-Ion Hyperfine Qubits, *Phys. Rev. Lett.* **117**, 060504 (2016).
- [4] J. P. Gaebler, T. R. Tan, Y. Lin, Y. Wan, R. Bowler, A. C. Keith, S. Glancy, K. Coakley, E. Knill, D. Leibfried, and D. J. Wineland, High-Fidelity Universal Gate Set for $^9\text{Be}^+$ Ion Qubits, *Phys. Rev. Lett.* **117**, 060505 (2016).
- [5] Y. Wang, M. Um, J. Zhang, S. An, M. Lyu, J. N. Zhang, L. M. Duan, D. Yum, and K. Kim, Single-qubit quantum memory exceeding ten-minute coherence time, *Nat. Photonics* **11**, 646 (2017).
- [6] M. A. Sepiol, A. C. Hughes, J. E. Tarlton, D. P. Nadlinger, T. G. Ballance, C. J. Ballance, T. P. Harty, A. M. Steane, J. F. Goodwin, and D. M. Lucas, Probing Qubit Memory Errors at the Part-per-Million Level, *Phys. Rev. Lett.* **123**, 110503 (2019).
- [7] D. Kielpinski, C. Monroe, and D. J. Wineland, Architecture for a large-scale ion-trap quantum computer, *Nature (London)* **417**, 709 (2002).
- [8] C. Monroe and J. Kim, Scaling the ion trap quantum processor, *Science* **339**, 1164 (2013).
- [9] J. Kim, P. Maunz, T. Kim, J. Hussman, R. Noek, A. Mehta, C. Monroe, T. Ralph, and P. K. Lam, Modular Universal Scalable Ion-trap Quantum Computer (MUSIQC), *AIP Conf. Proc.* **1363**, 190 (2011).
- [10] H. M. Meyer, R. Stockill, M. Steiner, C. Le Gall, C. Matthiesen, E. Clarke, A. Ludwig, J. Reichel, M. Atatüre, and M. Köhl, Direct Photonic Coupling of a Semiconductor Quantum Dot and a Trapped Ion, *Phys. Rev. Lett.* **114**, 123001 (2015).
- [11] H. J. Kimble, The quantum internet, *Nature (London)* **453**, 1023 (2008).
- [12] A. Broadbent, J. Fitzsimons, and E. Kashefi, Universal blind quantum computation (2009) pp. 517–526.
- [13] V. M. Schäfer, C. J. Ballance, K. Thirumalai, L. J. Stephenson, T. G. Ballance, A. M. Steane, and D. M. Lucas, Fast quantum logic gates with trapped-ion qubits, *Nature (London)* **555**, 75 (2018).
- [14] A. Walther, F. Ziesel, T. Ruster, S. T. Dawkins, K. Ott, M. Hettrich, K. Singer, F. Schmidt-Kaler, and U. Poschinger, Controlling Fast Transport of Cold Trapped Ions, *Phys. Rev. Lett.* **109**, 080501 (2012).
- [15] R. Bowler, J. Gaebler, Y. Lin, T. R. Tan, D. Hanneke, J. D. Jost, J. P. Home, D. Leibfried, and D. J. Wineland, Coherent Diabatic Ion Transport and Separation in a Multizone Trap Array, *Phys. Rev. Lett.* **109**, 080502 (2012).
- [16] C. Monroe, R. Raussendorf, A. Ruthven, K. R. Brown, P. Maunz, L.-M. Duan, and J. Kim, Large-scale modular quantum-computer architecture with atomic memory and photonic interconnects, *Phys. Rev. A* **89**, 022317 (2014).
- [17] D. Hucul, I. V. Inlek, G. Vittorini, C. Crocker, S. Debnath, S. M. Clark, and C. Monroe, Modular entanglement of atomic qubits using photons and phonons, *Nat. Phys.* **11**, 37 (2015).
- [18] P. C. Humphreys, N. Kalb, J. P. J. Morits, R. N. Schouten, R. F. L. Vermeulen, D. J. Twitchen, M. Markham, and R. Hanson, Deterministic delivery of remote entanglement on a quantum network, *Nature (London)* **558**, 268 (2018).
- [19] R. Stockill, M. J. Stanley, L. Huthmacher, E. Clarke, M. Hugues, A. J. Miller, C. Matthiesen, C. Le Gall, and M. Atatüre, Phase-Tuned Entangled State Generation between Distant Spin Qubits, *Phys. Rev. Lett.* **119**, 010503 (2017).
- [20] M. Lettner, M. Mücke, S. Riedl, C. Vo, C. Hahn, S. Baur, J. Bochmann, S. Ritter, S. Dürr, and G. Rempe, Remote Entanglement between a Single Atom and a Bose-Einstein Condensate, *Phys. Rev. Lett.* **106**, 210503 (2011).
- [21] S. Ritter, C. Nölleke, C. Hahn, A. Reiserer, A. Neuzner, M. Uphoff, M. Mücke, E. Figueroa, J. Bochmann, and G. Rempe, An elementary quantum network of single atoms in optical cavities, *Nature (London)* **484**, 195 (2012).
- [22] B. Hensen, H. Bernien, A. E. Dréau, A. Reiserer, N. Kalb, M. S. Blok, J. Ruitenbergh, R. F. L. Vermeulen, R. N. Schouten, C. Abellán, W. Amaya, V. Pruneri, M. W. Mitchell, M. Markham, D. J. Twitchen, D. Elkouss, S. Wehner, T. H. Taminiau, and R. Hanson, Loophole-free Bell inequality violation using electron spins separated by 1.3 kilometres, *Nature (London)* **526**, 682 (2015).
- [23] M. Żukowski, A. Zeilinger, M. A. Horne, and A. K. Ekert, Event-ready-detectors’ Bell experiment via entanglement swapping, *Phys. Rev. Lett.* **71**, 4287 (1993).
- [24] R. Nigmatullin, C. J. Ballance, N. D. Beaudrap, and S. C. Benjamin, Minimally complex ion traps as modules for quantum communication and computing, *New J. Phys.* **18**, 103028 (2016).
- [25] B. B. Blinov, D. L. Moehring, L. M. Duan, and C. Monroe, Observation of entanglement between a single trapped atom and a single photon, *Nature (London)* **428**, 153 (2004).
- [26] D. L. Moehring, P. Maunz, S. Olmschenk, K. C. Younge, D. N. Matsukevich, L.-M. Duan, and C. Monroe, Entanglement of single-atom quantum bits at a distance, *Nature (London)* **449**, 68 (2007).
- [27] C. Simon and W. T. M. Irvine, Robust Long-Distance Entanglement and a Loophole-Free Bell Test with Ions and Photons, *Phys. Rev. Lett.* **91**, 110405 (2003).
- [28] Sandia National Laboratories HOA2.
- [29] A. H. Myerson, D. J. Szwer, S. C. Webster, D. T. C. Allcock, M. J. Curtis, G. Imreh, J. A. Sherman, D. N. Stacey, A. M. Steane, and D. M. Lucas, High-Fidelity Readout of Trapped-Ion Qubits, *Phys. Rev. Lett.* **100**,

- 200502 (2008).
- [30] ARTIQ Sinara hardware, <https://m-labs.hk/experiment-control/sinara-core/>.
- [31] Laser Components COUNT BLUE, quantum efficiency measured at 422 nm.
- [32] L. J. Stephenson, *Entanglement between nodes of a quantum network*, Ph.D. thesis, University of Oxford (2019).
- [33] See Supplemental Material for a more detailed discussion of methods and data analysis.
- [34] P. Badziąg, M. Horodecki, P. Horodecki, and R. Horodecki, Local environment can enhance fidelity of quantum teleportation, *Phys. Rev. A* **62**, 012311 (2000).
- [35] G. Shu, N. Kurz, M. R. Dietrich, and B. B. Blinov, Efficient fluorescence collection from trapped ions with an integrated spherical mirror, *Phys. Rev. A* **81**, 042321 (2010).
- [36] M. Fischer, M. Bader, R. Maiwald, A. Golla, M. Sondermann, and G. Leuchs, Efficient saturation of an ion in free space, *Applied Physics B* **117**, 797 (2014).
- [37] J. I. Cirac, P. Zoller, H. J. Kimble, and H. Mabuchi, Quantum State Transfer and Entanglement Distribution among Distant Nodes in a Quantum Network, *Phys. Rev. Lett.* **78**, 3221 (1997).
- [38] T. Kim, P. Maunz, and J. Kim, Efficient collection of single photons emitted from a trapped ion into a single-mode fiber for scalable quantum-information processing, *Phys. Rev. A* **84**, 063423 (2011).
- [39] A. Stute, B. Casabone, P. Schindler, T. Monz, P. O. Schmidt, B. Brandstätter, T. E. Northup, and R. Blatt, Tunable ionphoton entanglement in an optical cavity, *Nature (London)* **485**, 482 (2012).
- [40] A. Stute, B. Casabone, B. Brandstätter, K. Friebe, T. E. Northup, and R. Blatt, Quantum-state transfer from an ion to a photon, *Nat. Photonics* **7**, 219 (2013).
- [41] T. A. Wright, R. J. A. Francis-Jones, C. B. E. Gawith, J. N. Becker, P. M. Ledingham, P. G. R. Smith, J. Nunn, P. J. Mosley, B. Brecht, and I. A. Walmsley, Two-Way Photonic Interface for Linking the Sr^+ Transition at 422 nm to the Telecommunication *C* Band, *Phys. Rev. Applied* **10**, 044012 (2018).
- [42] S. Benjamin (private communication).
- [43] S. Bourdeauducq *et al.*, m-labs/artiq: 4.0 (Version 4.0) (2018).

Supplemental material for ‘High-rate, high-fidelity entanglement of qubits across an elementary quantum network’

L. J. Stephenson,* D. P. Nadlinger,* B. C. Nichol, S. An, P. Drmota,
T. G. Ballance,† K. Thirumalai, J. F. Goodwin, D. M. Lucas, and C. J. Ballance‡
Department of Physics, University of Oxford, Clarendon Laboratory, Parks Road, Oxford OX1 3PU, U.K.
(Dated: May 12, 2020)

S1. PHOTON COLLECTION

To collect 422 nm photons emitted by the two ions, custom-designed lens objectives manufactured by Photon Gear [1] are used. They provide near-diffraction-limited performance at an input-side numerical aperture of 0.6 (specified: ≤ 0.08 waves rms at 403.1 nm). The image-side numerical aperture is 0.09, designed to match the ion emission into standard, commercially available step-index fused-silica fibres.

The objective lens is mounted on a five-axis stage for fine control over translational and rotational alignment. After fitting the observed point spread function with a low-order Zernike polynomial model similar to ref. [2], a cylindrical lens is inserted near the image plane to correct for residual aberrations likely caused by varying thickness across the vacuum viewport.

The tip of the collection fibre is mounted on a three-axis positioning stage, which can be adjusted using open-loop piezo actuators to correct for mechanical relaxation and slow, thermal drifts. Automatically tracking the optimum in observed fluorescence count rate allows us to retain good fibre-coupling efficiency over many days. (The short-term passive stability of the system was sufficient for typical experiments, such as the for the data presented in the main text, to be conducted without interruptions for realignment.)

S2. ION-PHOTON TOMOGRAPHY

In the following, we discuss the experiments performed to separately characterise the ion-photon interface of each ion trap node, that is, the quantum state tomography measurements of the joint ion-photon state following picosecond laser excitation.

To implement the necessary measurements on the photonic state, we use the same Bell state analyser apparatus as for the remote entanglement experiment (see Fig. 3 in the main manuscript), but allow only light from one trap to enter the system. We determine the fast axes and retardances of the individual waveplates separately, and then run the experiment while varying their orientation in a motorised mount, reading out the ion state after a click has been observed on APD0.

We choose to analyse the ion state for all combinations of fast-axis angles of $\{0, \pi/4\}$ for the quarter-wave plate,

and $\{0, \pi/8, \pi/4, 3\pi/8\}$ for the half-wave plate, defined with respect to the measurement polariser. This implements an over-complete set of projectors for measuring the photonic state. (For ideal waveplates, several of these choices would give rise to the same measurement projector.)

To analyse the ion state, we execute a sequence of 674 nm laser pulses to map part of the population into $|D_{5/2}, m=-3/2\rangle$ and optionally apply extra $\pi/2$ -rotations around an axis in the xy plane. As the phase of the ion-photon state in the laboratory frame is set with the detection of the photon, these analysis sequences are triggered at a fixed time offset from the avalanche photodetector click (with ~ 1 ns precision).

The results from two such tomography runs for Alice and Bob are shown in Fig. S1. In total, 624 000 (572 000) copies of the ion-photon state were measured in Alice (Bob) for these datasets, distributed over 27 min (18 min) of wall clock time. The density matrix estimates are obtained by direct numerical optimisation of the likelihood function over the $15 + 1$ real degrees of freedom parameterising the state and the overall collection efficiency. From those estimates, the fully entangled fraction [3], that is, the fidelity to the nearest maximally entangled state, is computed as 97.90(12)% and 97.70(12)%, respectively, where the errors are given as the s.e.m. obtained from parametric bootstrapping.

We make no attempt to control the polarisation rotation introduced by the single-mode fibre linking the ion traps with the polarisation state analyser setup. This results in an extra, a priori unknown, unitary transformation on the photonic part of the observed state. An arbitrary choice of phase reference is also made for the ion’s state. To aid visual interpretation, the same MLE density matrix results are hence shown in Fig. S2 after post-processing with local rotations to maximise their overlap with $|\Phi^+\rangle := (|\downarrow H\rangle + |\uparrow V\rangle) / \sqrt{2}$. Drifts in birefringence due to ambient temperature and mechanical stress lead to slow changes in the unitary induced by the fibre, but we typically observe it to be stable to $\gtrsim 99\%$ in state overlap over many days.

Imperfections in the 674 nm laser pulses and ion qubit decoherence due to magnetic field noise are expected to have a significant effect on the observed ion-photon correlations (see main text). While these effects can be characterised separately, we do not adjust the measurement projectors assumed in the tomography analysis for any such

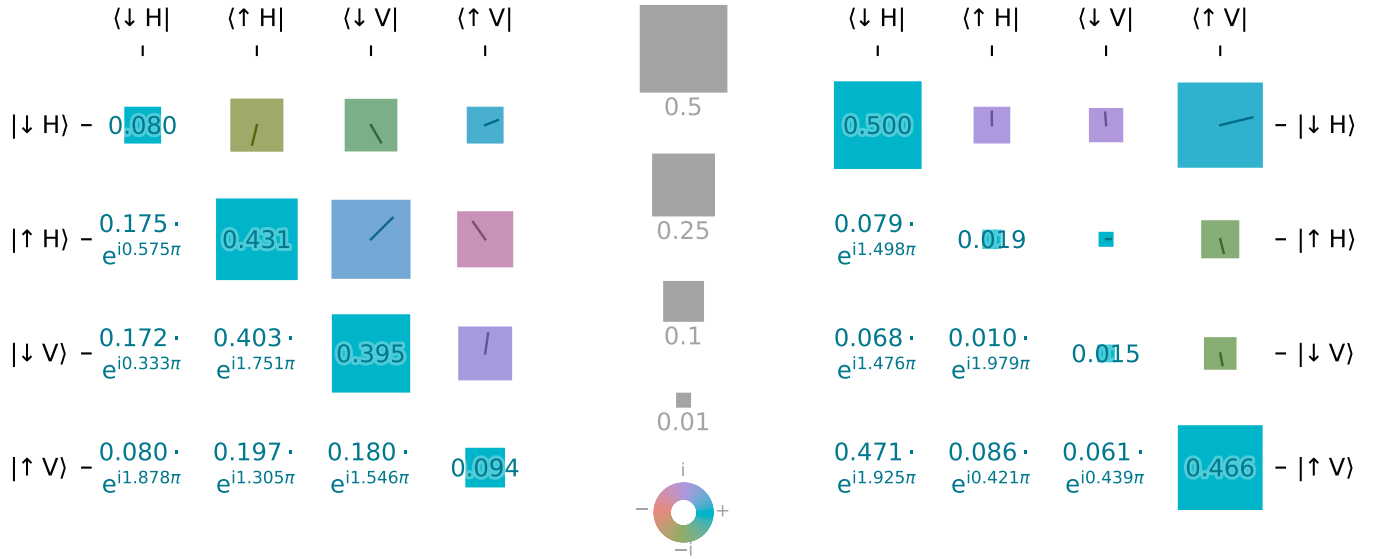


FIG. S1. Maximum-likelihood estimates of the joint ion-photon state produced in nodes Alice (*left*) and Bob (*right*), obtained from 624 000 and 572 000 individual state tomography measurements, respectively. The fully entangled fractions are $\mathcal{F}_{\text{Alice}} = 97.90(12)\%$ and $\mathcal{F}_{\text{Bob}} = 97.70(12)\%$, respectively, with the error given as the s.e.m. from parametric bootstrapping.

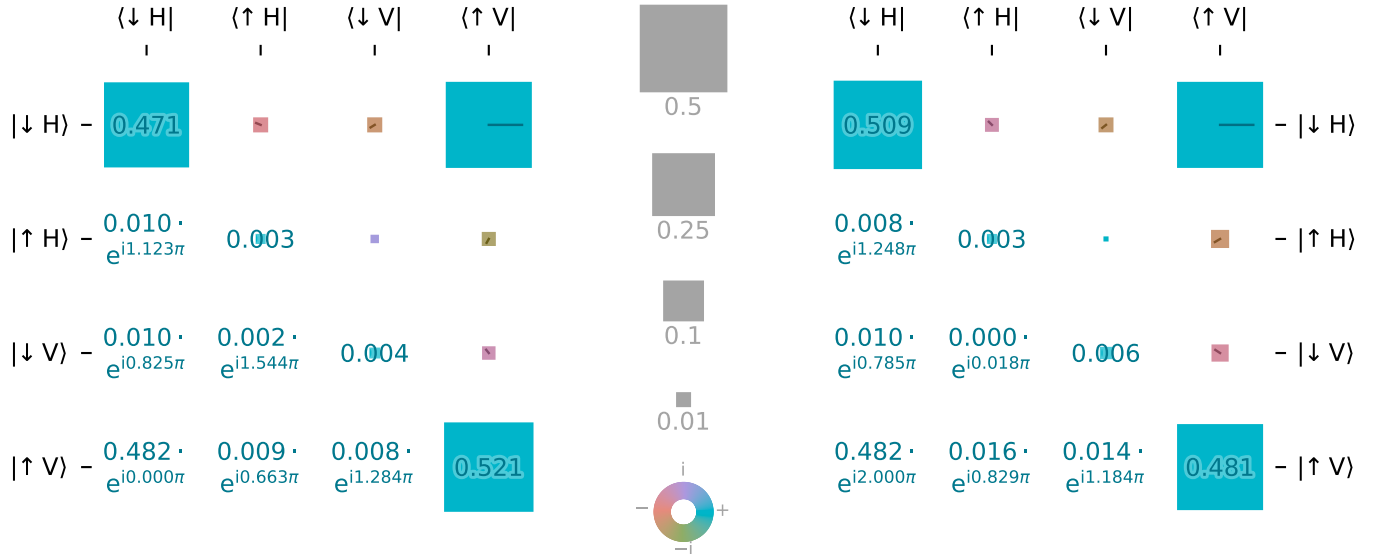


FIG. S2. Maximum-likelihood ion-photon state estimates in nodes Alice (*left*) and Bob (*right*) from Fig. S1, transformed post-hoc with unitary operations acting locally on the two subsystems to maximise the overlap with the Bell state $|\Phi^+\rangle := (|\downarrow H\rangle + |\uparrow V\rangle)/\sqrt{2}$.

errors (nor for imperfect state discrimination). As such, the tomographic estimate provides only a lower bound for the isolated performance of the ion-photon interface.

S3. ION-ION TOMOGRAPHY

In the main text, we present a performance evaluation of the photonic entanglement generation procedure using tomography of the joint ion-ion quantum state.

To obtain tomography data, we first set the orientation of the waveplate pairs on the input to the Bell state analyser apparatus to compensate the birefringence of

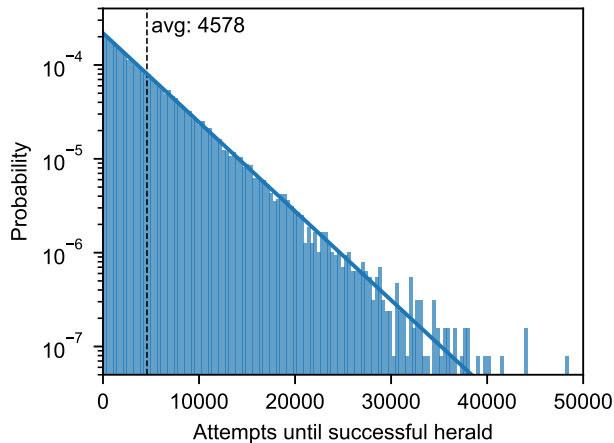


FIG. S3. Histogram of the number of excitation attempts necessary until a two-photon herald event was observed during acquisition of the ion-ion state tomography data presented in the main text. The solid line shows the exponential distribution corresponding to a Poisson process with success probability $1/4578 = 2.18 \times 10^{-4}$. The effective attempt rate is 833 kHz after including the amortised cost of periodic cooling operations, resulting in an average remote entanglement generation rate of 182 s^{-1} .

the fibre-optical links. We do this ahead-of-time in separate experiments by iteratively optimising the waveplate orientations for each node to maximise the probability of obtaining the ion $|\downarrow\rangle$ state after detecting a photon on APD0. This way, the polarisations incident on the non-polarising beam splitter for either decay channel are matched. Choosing equal Zeeman qubit frequencies by equalising the magnetic field strengths then removes any dependence of the resulting state on the photon detection times.

The state of each ion qubit is measured along the x -, y - or z -axis of the Bloch sphere, giving rise to nine possible measurement settings, each corresponding to a projective measurement onto the four eigenvectors of a tensor product of Pauli matrices. For the data presented in the main text, each measurement is performed on 1000 heralded states. For each attempt, we permit all four heralding detector combinations and record which occurred, to later separate them for data analysis [4]. We iterate four times through a random permutation of basis combinations, analysing a total of 36 000 ion-ion states.

In total, the data acquisition time was approximately 10 min. A total of 165 321 248 entanglement attempts were made, with the individual number of trials until success well-described by an exponential distribution, shown in Fig. S3.

To obtain an estimate for the quantum state of the system conditioned on each of the four detector click patterns, we perform maximum-likelihood state tomography

using a diluted fixed point iteration algorithm [5], which we also verify using direct numerical maximisation of the likelihood function. The resulting density matrices are in good agreement with the observed correlations; a comparison of observations and model is shown in Fig. S5. (There is a slight imbalance of observation counts between the four click patterns due to small differences in detector efficiencies.)

The quoted figures of merit (fidelity $\mathcal{F} = 0.940(5)$, entanglement of formation $E_F = 0.838(16)$) are computed from the density matrices and averaged over the detector click patterns. To estimate the statistical error, both parametric bootstrapping (simulated experiments from the MLE density matrices) and non-parametric bootstrapping (resampling of the experimental outcomes) are used, and found to give indistinguishable results; quoted as the s.e.m. above and in the main text. The size of the confidence intervals was also verified against a Bayesian model [6], in which a Hilbert–Schmidt uniform prior for the density matrix is assumed and the posterior distribution for each figures of merit is sampled using a Markov-chain Monte-Carlo algorithm (Metropolis–Hastings, using the implementation from ref. [7]).

No attempt was made to correct for the known qubit manipulation and state readout imperfections, which are a consequence of technical noise as discussed in the main text. As such, the quoted fidelities describe the whole-system performance and should be regarded as an upper bound for the link error.

* These two authors contributed equally

† Present address: ColdQuanta UK Ltd, Oxford

‡ chris.ballance@physics.ox.ac.uk

- [1] Photon Gear Inc., Ontario, NY, United States.
- [2] J. D. Wong-Campos, K. G. Johnson, B. Neyenhuis, J. Mizrahi, and C. Monroe, High-resolution adaptive imaging of a single atom, *Nat. Photonics* **10**, 606 (2016).
- [3] P. Badziąg, M. Horodecki, P. Horodecki, and R. Horodecki, Local environment can enhance fidelity of quantum teleportation, *Phys. Rev. A* **62**, 012311 (2000).
- [4] This separation is merely to diagnose unexpected differences between the herald patterns; in an application making use of the remotely entangled state, the click pattern dependence would immediately be corrected by inserting additional local phase rotations into the computation as necessary.
- [5] J. Reháček, Z. Hradil, E. Knill, and A. I. Lvovsky, Diluted maximum-likelihood algorithm for quantum tomography, *Phys. Rev. A* **75**, 042108 (2007).
- [6] P. Faist and R. Renner, Practical and Reliable Error Bars in Quantum Tomography, *Phys. Rev. Lett.* **117**, 010404 (2016).
- [7] P. Faist, The tomographer project, v5.4 (2018).

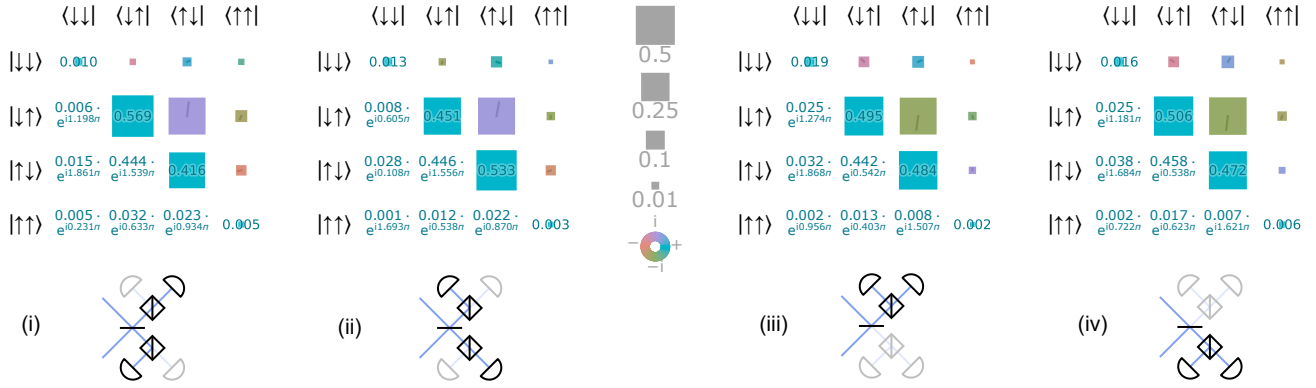


FIG. S4. Maximum-likelihood ion-ion state estimates heralded by the four different photon detector click patterns. (This is a duplicate of Fig. 4 in the main text, but with the magnitude and phase of the matrix elements shown numerically.)

O_A	O_B	$+A+B$	$-A+B$	$+A-B$	$-A-B$
Z	Z	4	424	564	10
Z	X	255	217	297	194
Z	Y	283	218	316	193
X	Z	212	222	271	263
X	X	259	236	227	289
X	Y	28	463	477	26
Y	Z	178	213	288	285
Y	X	424	32	32	524
Y	Y	249	223	193	295

(i) Number of observations per Pauli eigenstate for detectors APD0 and APD2, for a total of 8884 clicks.

O_A	O_B	$+A+B$	$-A+B$	$+A-B$	$-A-B$
Z	Z	3	533	425	11
Z	X	210	256	233	287
Z	Y	204	294	232	252
X	Z	263	278	235	231
X	X	273	239	228	332
X	Y	38	508	425	26
Y	Z	254	280	267	250
Y	X	451	30	27	495
Y	Y	287	233	180	312

(ii) Number of observations per Pauli eigenstate for detectors APD1 and APD3, for a total of 9082 clicks.

O_A	O_B	$+A+B$	$-A+B$	$+A-B$	$-A-B$
Z	Z	1	449	459	18
Z	X	206	259	249	236
Z	Y	247	260	224	185
X	Z	234	237	260	251
X	X	224	250	257	192
X	Y	467	28	30	399
Y	Z	221	249	220	263
Y	X	21	441	450	36
Y	Y	227	301	259	202

(iii) Number of observations per Pauli eigenstate for detectors APD0 and APD1, for a total of 8512 clicks.

O_A	O_B	$+A+B$	$-A+B$	$+A-B$	$-A-B$
Z	Z	5	531	544	19
Z	X	270	321	292	218
Z	Y	271	278	309	234
X	Z	262	236	282	263
X	X	221	264	295	214
X	Y	535	21	29	500
Y	Z	240	261	242	289
Y	X	20	511	482	24
Y	Y	240	305	267	227

(iv) Number of observations per Pauli eigenstate for detectors APD2 and APD3, for a total of 9522 clicks.

TABLE S1. Number of observations of each eigenstate for all tensor-product combinations $O_A \otimes O_B$ of Pauli operators in the ion-ion tomography experiment, for each of the four heralding detector patterns. This constitutes the complete input to the maximum-likelihood estimation procedure used to derive the density matrices presented the main text and Fig. S4 (and, by extension, the quoted fidelities).

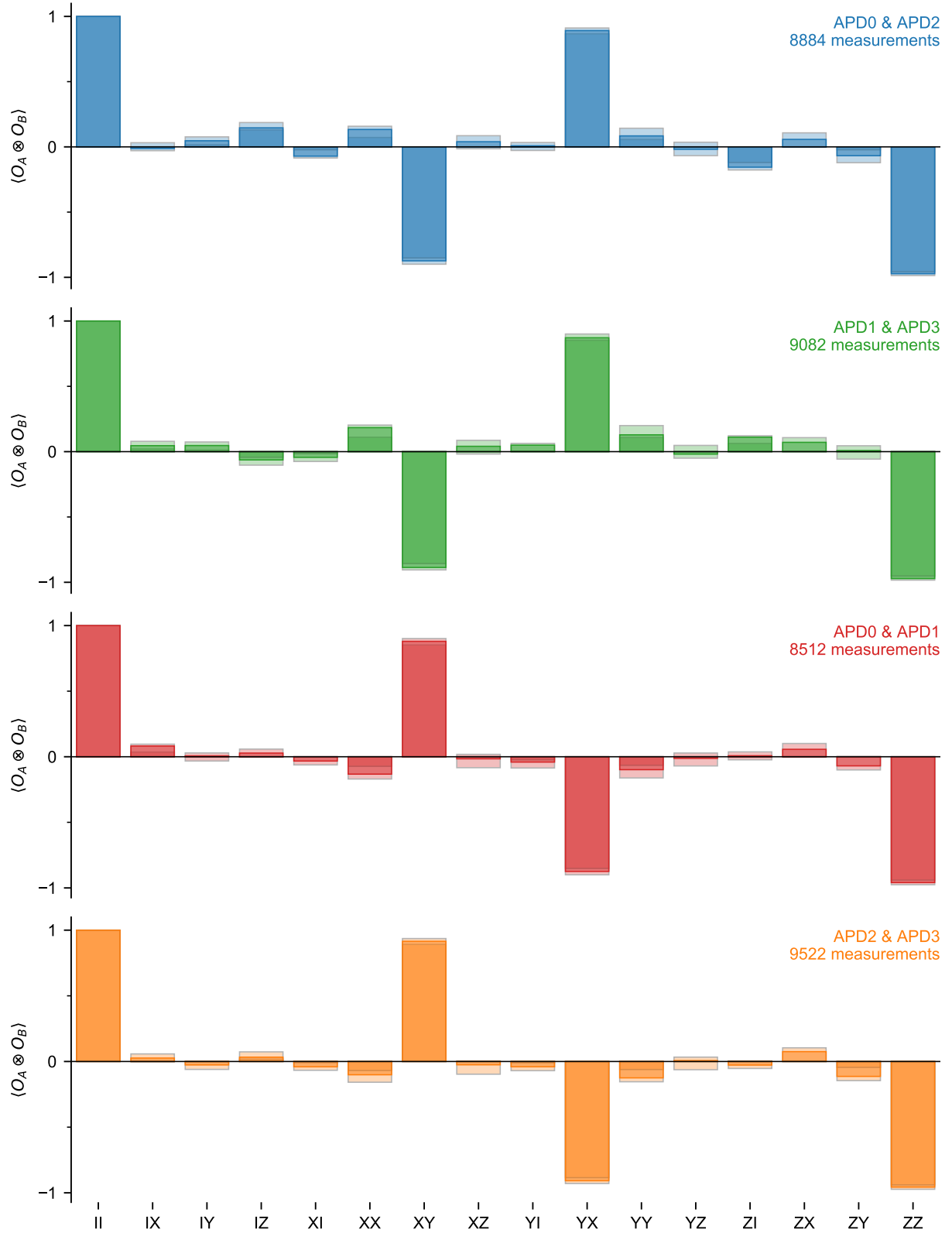


FIG. S5. Ion-ion tomography data for the states heralded by the four different photon detector click patterns. For each two-qubit Pauli operator, the solid bars show the experimental measurements (averages directly computed from the raw data from Table S1), whereas transparent bars denote the 95% confidence interval of the respective expected value from the maximum-likelihood tomography estimate (obtained via bootstrapping).